



Cite this: *Dalton Trans.*, 2024, **53**, 6451

## Molecularly-induced roughness and oxidation in cobalt/organodithiol/cobalt nanolayers synthesized by sputter-deposition and molecular sublimation†

Collin Rowe, <sup>b</sup> Sathish Kumar Shanmugham, <sup>a</sup> Grzegorz Greczynski, <sup>a</sup> Lars Hultman, <sup>a</sup> Arnaud le Febvrier, <sup>a</sup> Per Eklund <sup>\*a</sup> and Ganpati Ramanath <sup>\*a,b</sup>

Integrating interfacial molecular nanolayers (MNL) with inorganic nanolayers is of interest for understanding processing-structure/chemistry correlations in hybrid nanolaminates. Here, we report the synthesis of Co/biphenyldithiol (BPDT)/Co nanolayer sandwiches by metal sputter-deposition and molecular sublimation. The density and surface roughness of the Co layers deposited on the native oxide are invariant with the Ar pressure  $p_{Ar}$  during deposition. In contrast, the Co layer roughness  $r_{Co}$  deposited on top of the BPDT MNL increases with  $p_{Ar}$ , and correlates with a higher degree of Co oxidation. Increased roughening is attributed to MNL-accentuated self-shadowing of low mobility Co atoms at high  $p_{Ar}$ , which consequently increases Co oxidation. These results indicating MNL-induced effects on the morphology and chemistry of the inorganic layers should be of importance for tailoring nanolayered hybrid interfaces and laminates.

Received 20th June 2023,  
Accepted 13th March 2024  
DOI: 10.1039/d3dt01910a  
[rsc.li/dalton](http://rsc.li/dalton)

## Introduction

Introducing molecular nanolayers (MNL) at inorganic interfaces<sup>1</sup> is an exciting strategy for enhancing a variety of properties.<sup>2</sup> Inorganic/MNL interfaces and multilayers are germane to applications in nanoelectronics,<sup>3</sup> thermoelectric refrigeration,<sup>4</sup> flexible<sup>5</sup> and bio-compatible<sup>6</sup> devices with novel optical,<sup>7</sup> mechanical,<sup>8,9</sup> and thermoelectric<sup>10,11</sup> responses. This approach is also relevant to synthesizing inorganic/organic hybrid laminates with unusual property combinations beyond that obtained in purely inorganic multilayers (e.g., superhardness<sup>12</sup>). For instance, recent theoretical calculations on multilayered stacks of Au/MNL/Au interfaces have indicated the possibility of emergent phenomena, such as viscoelastic bandgaps.<sup>13</sup> Metal–oxide multilayers<sup>14,15</sup> with interfacial MNLs can simultaneously exhibit optical transparency, high electrical and low thermal conductance, with mechanical flexibility.<sup>7,16</sup>

Hybrid multilayer composites with alternating organic and inorganic nanolayers are typically synthesized by combining atomic and molecular layer deposition.<sup>17,18</sup> Since low-temperature deposition of inorganic layers is necessary to preserve the integrity of the MNL during synthesis of nanolayered inorganic–organic composites, there is interest in harnessing energetic particles during deposition to get good quality inorganic layers. While MNLs can be formed by wet-chemical self-assembly on inorganic surfaces,<sup>19–21</sup> combining MNL formation with inorganic film deposition methods entailing vacuum breaks and repeated substrate loading/unloading compromise control over the interface chemistry and are not easily scalable.

Here, we report the synthesis of Co/biphenyldithiol (BPDT) MNL/Co nanolayer thin-film sandwiches using a combination of metal sputter-deposition and sublimation of the BPDT molecules without atmosphere exposure. Co nanolayers deposited on top of a BPDT MNL exhibit a higher roughness than Co nanolayers deposited directly on  $\text{SiO}_2$ , *i.e.*, without an MNL. Furthermore, MNL-induced roughening correlates with a higher degree of cobalt oxidation, both of which are accentuated at higher Co deposition pressures. This knowledge would be essential for the design and synthesis of inorganic–organic nanolaminates with emergent properties, *e.g.*, transparent electrical conductors,<sup>7</sup> flexible thermoelectrics,<sup>22,23</sup> and smart materials with mechanical bandgaps.<sup>4,9</sup>

<sup>a</sup>Thin Film Physics Division, Department of Physics, Chemistry and Biology (IFM), Linköping University, SE-58222 Linköping, Sweden. E-mail: [per.eklund@liu.se](mailto:per.eklund@liu.se), [Ramanath@rpi.edu](mailto:Ramanath@rpi.edu)

<sup>b</sup>Rensselaer Polytechnic Institute, Department of Materials Science and Engineering, Troy, NY 12180, USA

† Electronic supplementary information (ESI) available. See DOI: <https://doi.org/10.1039/d3dt01910a>



## Experimental details

We synthesized Co/MNL/Co sandwiches (see Fig. 1a inset) with the interfacial MNL comprised of biphenyl 4,4'-dithiol (BPDT)<sup>24</sup> in a  $1.7 \times 10^{-7}$  Pa base pressure UHV system described elsewhere.<sup>25</sup> The main chamber was used for sputter-deposition, and the load-lock chamber was used for MNL sublimation (see ESI†). The substrates consisting of 10 mm  $\times$  10 mm pieces of Si(001) with a  $\sim$ 3 nm-thick native oxide layer were ultrasonically cleaned with acetone and isopropanol for 10 minutes and blow-dried with N<sub>2</sub>. The substrate pieces were inserted into the main chamber through the load-lock for magnetron sputter-deposition of Co layers from a 50 mm-diameter Co target (99.5% purity). Immediately prior to deposition, the Co targets were sputter-cleaned for 20 minutes.

The Co film deposition rate and time were determined for different Ar pressures in the  $0.20 \leq p_{Ar} \leq 3.2$  Pa range. The substrates were placed on an electrically floating holder placed 140 mm from the Co sputter target. The first Co (bottom) layer was sputter deposited using 15 W dc power plasma. For BPDT MNL formation on the first (bottom) Co layer, the Co/SiO<sub>2</sub>/Si

structures were transferred to the load-lock and exposed to BPDT flux from a crucible containing  $\sim$ 100 mg BPDT powder (95% purity, Aldrich). The load-lock pressure was held above 0.4 Pa during transfer. BPDT molecules were sublimed for 30 minutes at  $\lesssim$ 0.3 Pa (ref. 26) and with the crucible temperature at  $T_{\text{sublimation}} = 45 \pm 5$  °C. The BPDT/Co/SiO<sub>2</sub>/Si structures were transferred back to the main chamber for sputter-depositing the Co overlayer on the BPDT MNL. For all Co/MNL/Co sandwiches, the targeted thicknesses of the bottom and top Co layers  $t_{Co}$  were 8 nm, and 4 nm, respectively.

Co film thickness and density were determined using Rutherford backscattering spectroscopy (RBS) and X-ray reflectivity (XRR) measurements. RBS data was acquired using a 2 MeV He<sup>2+</sup> beam incident at 5° to the surface normal, with the detector placed at a 170° scattering angle, and fit using SIMNRA simulations<sup>27,28</sup> of model structures. XRR measurements were carried out in a Rigaku Smartlab diffractometer with Cu K $\alpha$  radiation, and the data was analyzed using the PANalytical X'Pert Reflectivity software.<sup>29</sup> The top Co layer roughness  $r_{Co}$  in the Co/MNL/Co sandwiches were measured by tapping-mode atomic force microscopy (AFM) with a Bruker Dimension 3100 instrument, and the data was analyzed with the WSxM software.<sup>30</sup>

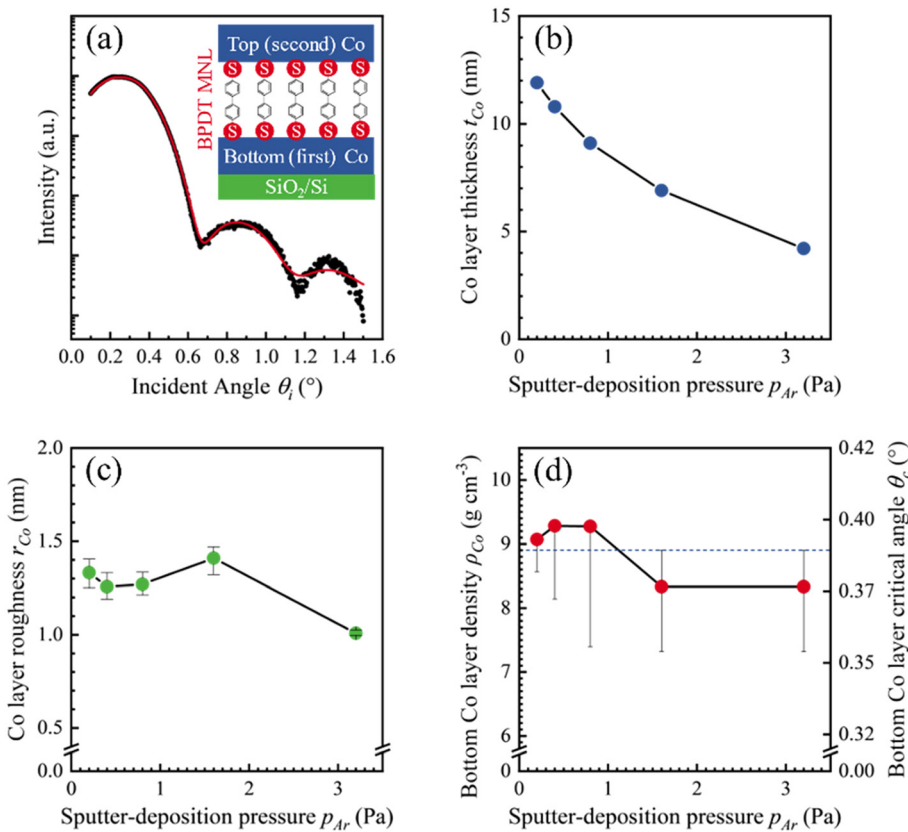


**Fig. 1** (a) XRR data overlaid with the best fit model (red curve) for a Co film deposited on SiO<sub>2</sub>/Si at  $p_{Ar} = 0.8$  Pa. The inset is a schematic of a Co/BPDT/Co thin film sandwich. The (b) thickness and (c) the Co layer roughness  $r_{Co}$  plotted as a function of  $p_{Ar}$ . The fitting uncertainties in  $t_{Co}$  are less than the symbol dimension representing each data point. (d)  $\rho_{Co}$  (left ordinate) obtained by  $\theta_c$  (right ordinate) determined from XRR data plotted as a function of  $p_{Ar}$ . The horizontal dashed line denotes both  $\rho_{Co}$  and  $\theta_c$  expected for bulk Co.



X-ray photoelectron spectroscopy (XPS) was used to study BPDT MNL formation in a Kratos Ultra DLD instrument ( $<1 \times 10^{-7}$  Pa base pressure) equipped with a monochromatic Al K $\alpha$  source. The pass energy was set to 160 eV for the survey scans and to 20 eV for higher energy resolution scans. Charging-induced shifts were corrected using the Co Fermi edge as the reference, and MultiPak<sup>31</sup> software was used for analysis. Raman spectra were obtained in a home-built system with a  $\sim 0.8 \mu\text{m}$  spot from a  $\sim 0.5 \text{ mW}$  532 nm solid-state laser, and a  $\sim 5.5 \text{ cm}^{-1}$  resolution detector.

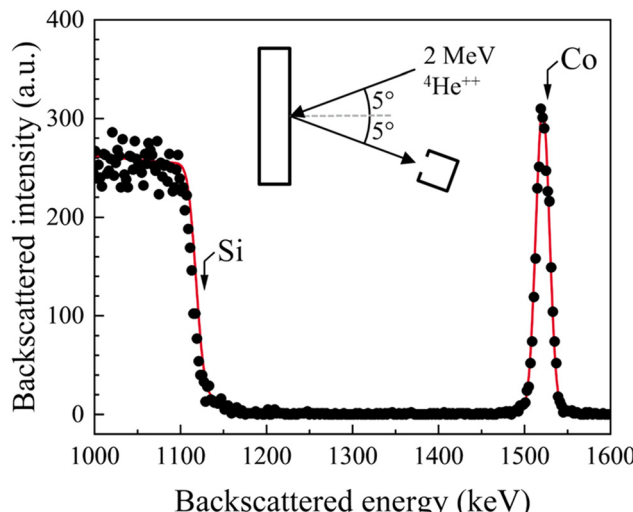


**Fig. 2** A representative RBS spectrum (points) and the SIMNRA simulation (line) from a Co film deposited at  $p_{\text{Ar}} = 0.8 \text{ Pa}$  (6 mTorr).

## Results and discussion

### The first Co layer on SiO<sub>2</sub>/Si

XRR data from Co-covered SiO<sub>2</sub>/Si(001) substrates were fit with simulated curves from Co/SiO<sub>2</sub>/Si models assuming homogenous densities and linear gradient interfaces (see Fig. 1a). XRR data analyses show that the nominal Co film thickness  $t_{\text{Co}}$  monotonically decreased with increasing Ar pressure  $p_{\text{Ar}}$  at which the Co film was sputter-deposited (Fig. 1b). We extracted  $t_{\text{Co}}$  from Kiessig fringe positions from simulations of model Co/SiO<sub>2</sub>/Si(001) structures of layers with different values of homogeneous densities. Our simulations also show that the Co layer RMS roughness<sup>32</sup> is in the  $1.0 \leq r_{\text{Co}} \leq 1.4 \text{ nm}$  range with no correlation with  $p_{\text{Ar}}$  (Fig. 1c). Analyses of the  $d/d\theta_i$  minima associated with the total-external reflection angle  $\theta_c$  (see ESI†) showed that the Co film density remained invariant with  $p_{\text{Ar}}$  at  $\rho_{\text{Co}}^{\text{XRR}} = 8.8 \pm 0.6 \text{ g cm}^{-3}$  (Fig. 1d).

SIMNRA fits of RBS spectra for Co/SiO<sub>2</sub>/Si model structures (e.g., see Fig. 2) yield an areal Co film density  $A_{\text{Co}} = 72 \times 10^{15} \text{ atoms cm}^{-2}$ . Dividing  $A_{\text{Co}}$  with  $t_{\text{Co}}$  obtained from XRR analyses yields a Co film density  $\rho_{\text{Co}}^{\text{RBS}} = 8.7 \pm 0.1 \text{ g cm}^{-3}$ , which is within 1% of the density  $\rho_{\text{Co}}^{\text{XRR}}$ . Additionally, dividing  $A_{\text{Co}}$  with  $\rho_{\text{Co}}^{\text{XRR}}$  yields  $t_{\text{Co}} = 8.0 \pm 0.6 \text{ nm}$ , which agrees well with  $t_{\text{Co}}$  determined from Kiessig fringes by XRR. These results confirm that the extracted values of  $t_{\text{Co}}$  and  $\rho_{\text{Co}}$  are self-consistent, with no observable changes in  $\rho_{\text{Co}}$ .

XPS spectra from Co films exposed to BPDT fluxes revealed S 2p core-level peaks<sup>33,34</sup> (Fig. 3a). Surprisingly, even as-deposited Co films showed S 2p peaks, albeit of lower intensity. This result indicates inadvertent BPDT exposure during sample residence and exchanges in the load-lock either

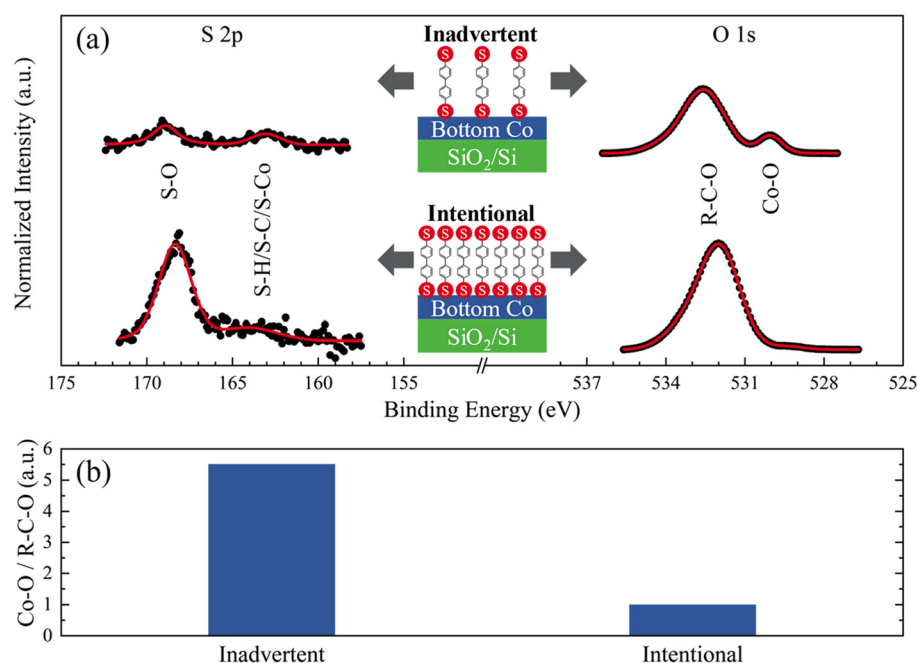


**Fig. 3** (a) S 2p and O 1s core-level spectra obtained by XPS at a  $\theta_{\text{SD}} = 45^\circ$  from Co films with inadvertent (top) and intended (bottom) BPDT exposure. (b) Co-O/R-C-O ratios derived from the O 1s spectra. All intensities are normalized to that of the Co 2p peak.



directly from the sublimation cell or refluxing from the load-lock chamber walls. Given the low BPDT vapor pressure,<sup>26</sup> this outcome was unexpected, and underscores the importance of using a shutter to physically isolate the molecular source during hybrid nanocomposites synthesis.

The O 1s contribution<sup>35–37</sup> associated with Co–O bonding is ~4-fold lower in Co films intentionally exposed to BPDT than in Co films with inadvertent BPDT exposure (Fig. 3b). This result indicates that BPDT MNL formed by intentional sublimation curtails Co oxidation considerably more than BPDT adsorption through inadvertent exposure, suggesting that inadvertent BPDT fluxes in our experiments do not result in continuous BPDT MNLs.

### Second Co layer deposition to synthesize Co/BPDT/Co sandwiches

XRR data from Co/BPDT/Co sandwiches with top Co layers deposited at  $0.2 \leq p_{Ar} \leq 3.2$  Pa exhibit two differential reflectivity minima (see ESI†) corresponding to  $\theta_c^{Co}$  and  $\theta_c^{Si}$  for  $0.2 \leq p_{Ar} \leq$

1.6 Pa. The data could not be fit with differential reflectivity curves generated from Co/BPDT/Co models with discrete layers. The similarity of the X-ray penetration depth and the film thicknesses in these structures confound the combined effects of even small changes in film roughness, thickness and composition, complicating meaningful interpretation.

The areal density of the top Co layer  $A_{Co}^{top}$  was determined by fitting RBS data from Co/BPDT/Co sandwiches (Fig. 4a) using  $t_{Co} = 8.1$  nm and  $A_{Co} = 72$  atoms  $\times 10^{15}$  cm $^{-2}$  for the bottom Co layer. These results show that the top Co layer  $A_{Co}$  monotonically decreases with increasing  $p_{Ar}$  (Fig. 4b). Our XRR results indicate that the Co density  $\rho_{Co}$  for the bottom layer is invariant for  $0.2 \leq p_{Ar} \leq 3.2$  Pa. If  $\rho_{Co}$  is similarly invariant for the top Co layer, and  $\rho_{Co}^{top} = \rho_{Co}^{bottom} = 8.8$  g cm $^{-3}$ , the top-layer Co thickness  $t_{Co}^{top} = \rho_{Co}^{RBS} / A_{Co}^{top}$  is estimated to be in the  $3.1 \leq t_{Co}^{top} \leq 4.7$  nm range. The mean  $t_{Co}^{top} = 3.9 \pm 0.7$  nm, which is close to the intended  $t_{Co}^{top} = 4$  nm.

AFM measurements of the top Co layer in the Co/BPDT/Co sandwiches (Fig. 5a) show a monotonic increase in root-mean-

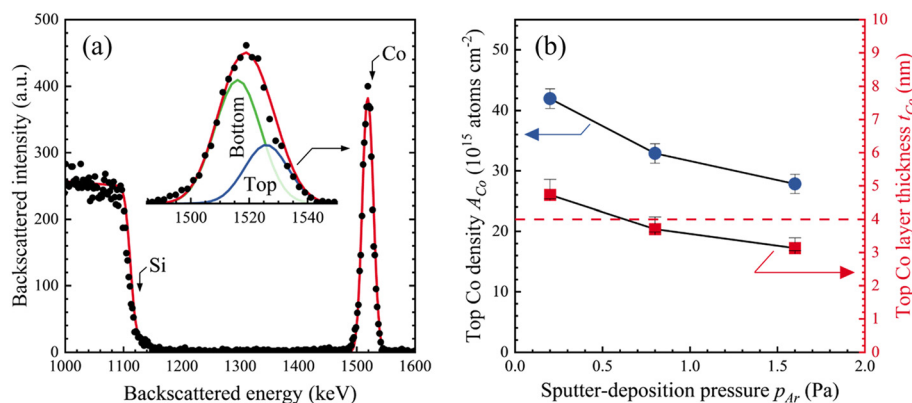


**Fig. 4** (a) The Co peak from a representative RBS spectrum fit with SIMNRA simulations (line) from a Co/BPDT/Co sandwich with the top Co layer deposited at  $p_{Ar} = 0.8$  Pa. Inset shows a magnified view of the Co peak, with the top and bottom Co layer contributions from simulations. (b) Areal density and thickness of the top Co nanolayer plotted versus  $p_{Ar}$ .

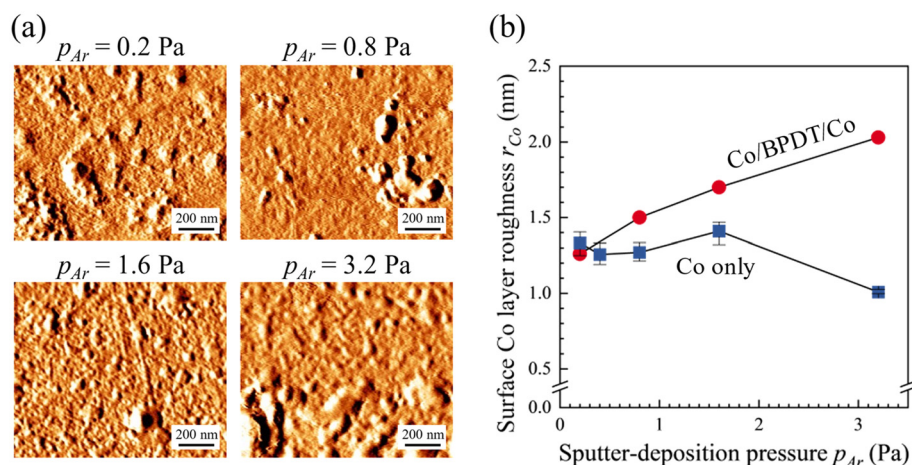


**Fig. 5** (a) AFM images from Co/BPDT/Co sandwiches for the top Co layer deposited at different  $p_{Ar}$ . (b) Top Co layer roughness in Co/BPDT/Co sandwiches (circles) and the bottom Co layer roughness in Co/SiO<sub>2</sub>/Si(001) structures (squares) plotted versus  $p_{Ar}$ . Roughness uncertainty is indicated by symbol size or error bar bounds, whichever is greater.



square roughness  $r_{\text{Co}}$  with  $p_{\text{Ar}}$  (Fig. 5b). Since the  $t_{\text{Co}}^{\text{bottom}}$  values are similar (within  $\pm 1.6$  nm) with only a slight decrease with  $p_{\text{Ar}}$ , the observed  $r_{\text{Co}}$  increase is clearly not a film thickness effect. The  $p_{\text{Ar}}-r_{\text{Co}}$  correlation seen in the top Co layer is absent in the bottom Co layer, as described earlier in section 3.1, and plotted in Fig. 5b for comparison. We thus infer that the higher roughness of the top Co layer in Co/BPDT/Co structures is due to the presence of the underlying BPDT MNL.

Higher frequency of gas-phase collisions expected with increasing  $p_{\text{Ar}}$  could promote higher roughness due to lowered adatom mobility resulting from lower average energy of sputtered species impinging on the surface at shallower angles. However, since this effect is not seen for the bottom Co layer deposited on  $\text{SiO}_2$ , we attribute the  $p_{\text{Ar}}-r_{\text{Co}}$  correlation in the top Co layer to the presence of the BPDT MNL. It appears that

the presence of an MNL accentuates the self-shadowing from low mobility of metal adatoms expected at higher  $p_{\text{Ar}}$  by virtue of the initial roughness caused by the BPDT layer. Thus, higher  $p_{\text{Ar}}$  leads to roughening for the top Co layer but not the bottom one grown on flat  $\text{SiO}_2$ . These observations suggest that the nature and extent of the MNL influence on the inorganic overlayer morphology are likely to be dependent on MNL chemistry and morphology.

XPS spectra recorded from Co/BPDT/Co sandwiches (see Fig. 6, and ESI<sup>†</sup>) indicate a correlation between Co oxidation and  $p_{\text{Ar}}$ , and corroborate BPDT adsorption on the top Co layer surface due to unintentional BPDT exposure discussed earlier. Co 2p peaks contain metallic  $\text{Co}^0$  as well as oxidized  $\text{Co}^{+2}$  and  $\text{Co}^{+3}$  contributions<sup>38–40</sup> (Fig. 6a). Assigning these non-zero oxidation states specifically to either Co–O or Co–S bonds is pre-

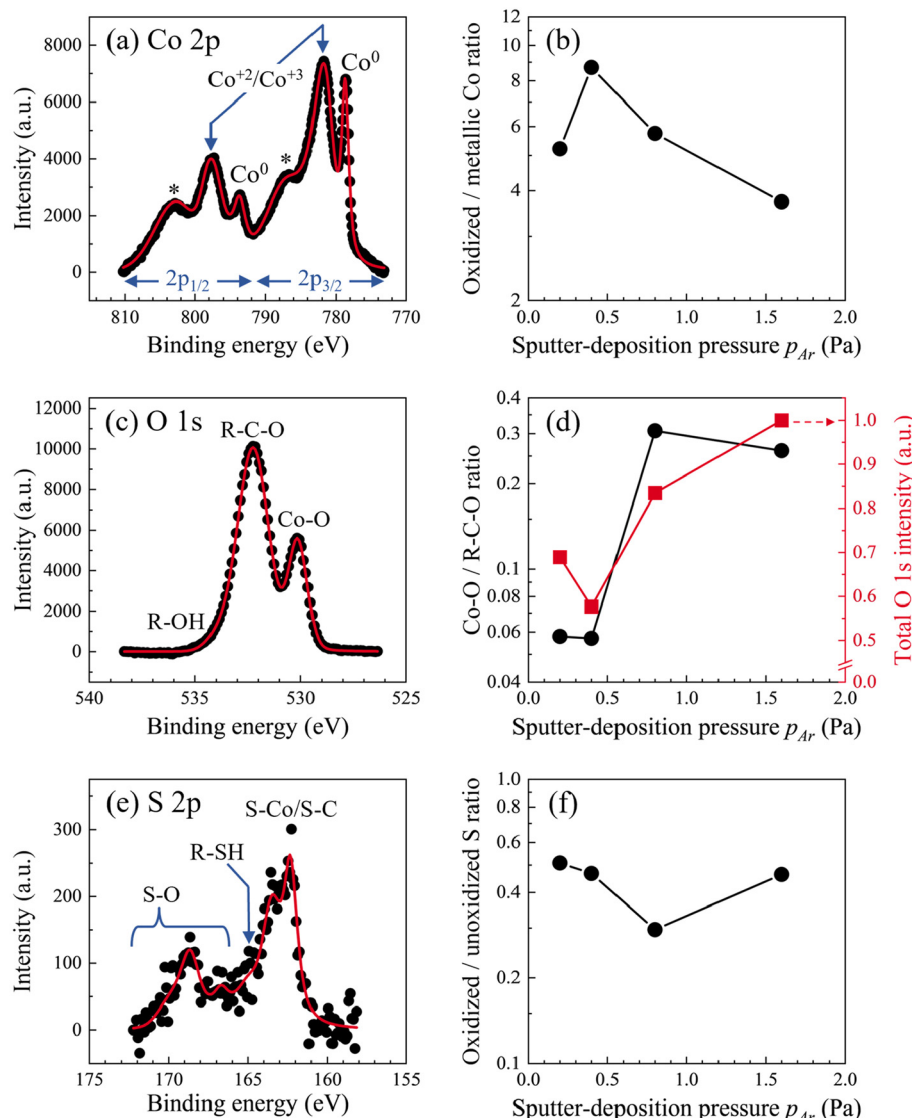
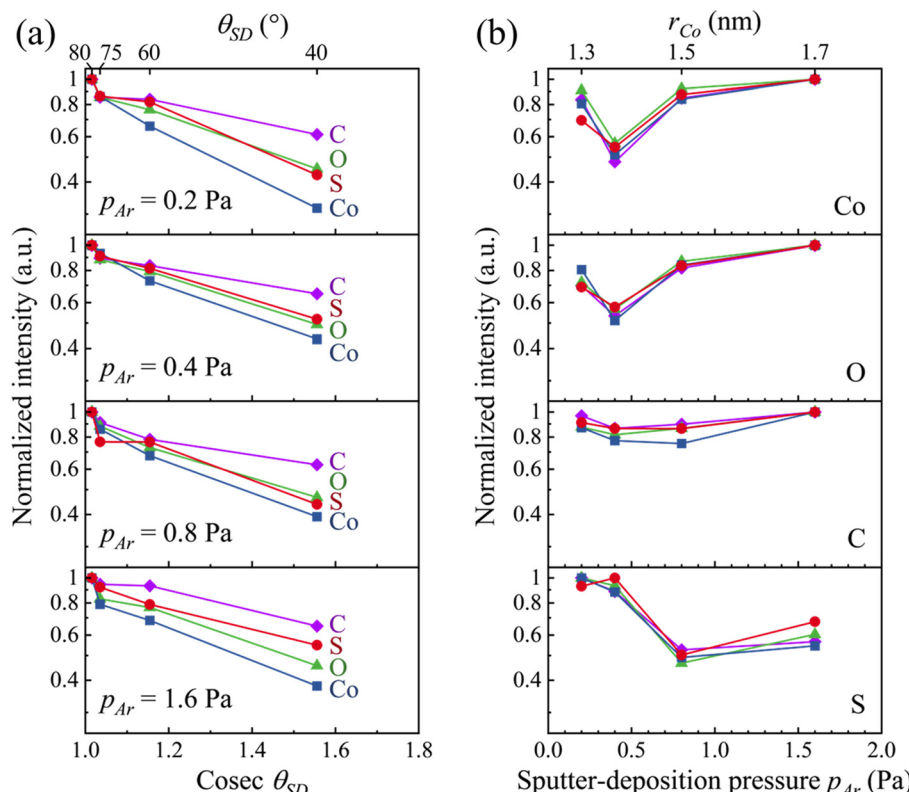


Fig. 6 (a) Co 2p, (c) O 1s and (e) S 2p spectra from Co/BPDT/Co nanolayers at  $\theta_{\text{SD}} = 60^\circ$ . In the Co 2p band, \* represents Co satellite peaks. Semi-log plots of sub-band intensity ratios from (b) Co 2p, (d) O 1s and (f) S 2p plotted as a function of  $p_{\text{Ar}}$ . The total O 1s band intensity is also shown on a linear scale (d, right axis). Detailed sub-band fittings are given in ESI.<sup>†</sup>





**Fig. 7** Normalized core-level peak intensities from XPS plotted versus (a) surface-to-detector angle  $\theta_{SD}$ , and (b) sputter-deposition pressure  $p_{Ar}$ . For each element, the intensities are normalized to that for  $\theta_{SD} = 80^\circ$  (in a), and normalized to the maximum intensity (in b) for each  $\theta_{SD}$ , namely,  $80^\circ$  (diamonds),  $75^\circ$  (triangles),  $60^\circ$  (circles), and  $40^\circ$  (squares).

cluded by overlaps in Co-S and Co-O signatures. The normalized oxidized/metallic Co peak ratio (Fig. 6b) does not exhibit any discernable trend with  $p_{Ar}$ .

Intensities of both the O 1s peak (Fig. 6c) and the O–Co sub-band<sup>35–37</sup> (Fig. 6d) increase with  $p_{Ar}$ , indicating that higher  $p_{Ar}$  is associated with a greater degree of oxidation of the top Co layer. Viewing this result alongside the  $p_{Ar}$ – $r_{Co}$  correlation for the top Co layer suggests a connection between Co layer roughness and the degree of Co oxidation to  $Co^{+2}$  or  $Co^{+3}$  states. The S 2p peak from adventitious BPDT are comprised of sub-bands from –SH, S–C, S–Co, and S–O moieties<sup>33,34</sup> (Fig. 6e). The sub-band in the 162–164 eV regime is labeled as S–Co/S–C because the S–Co and S–C states were indistinguishable in our measurements limited by  $\sim 1$  eV spectral resolution in our measurements. The high-binding energy sub-bands from a small fraction of S–O bonds are not captured in the O 1s spectra because of vast differences in the relative intensities of O 1s and S 2p peaks (see Fig. 6c & e and survey spectra in ESI†). The oxidized/unoxidized S (Fig. 6f) ratio does not exhibit any discernable trend with  $p_{Ar}$ .

Variable take-off angle XPS measurements show that the C 1s peak attenuates the least and Co 2p peaks attenuate the most with increasing surface-to-detector angle  $\theta_{SD}$  (Fig. 7a). These results indicate<sup>41</sup> that a C layer covers the top Co layer, with oxygen and sulfur straddled in between. For all  $\theta_{SD}$ , the

Co 2p and O 1s intensity attenuation trends with  $p_{Ar}$  appear to be correlated (Fig. 7b), consistent with increased Co oxidation at high  $p_{Ar}$ . The C 1s band intensity attenuation is insensitive to  $p_{Ar}$ , and the S 2p band mimics this for  $p_{Ar} < 0.4$  Pa. At

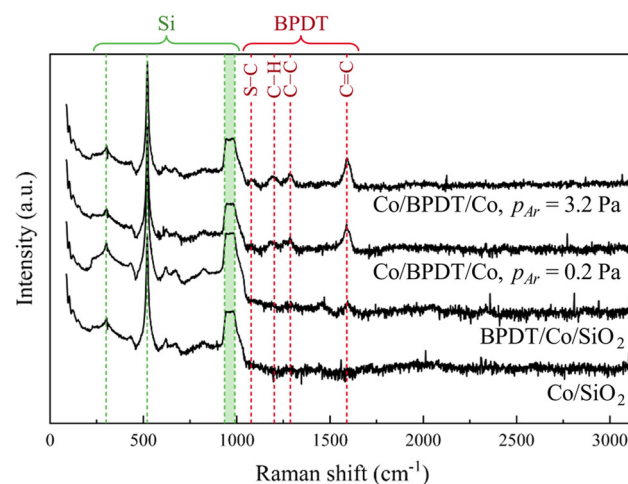


**Fig. 8** Raman spectra from the Co layer before and after BPDT exposure, and from Co/BPDT/Co sandwiches plotted on a semi-log plot. For the bottom Co layer  $p_{Ar} = 0.8$ .



higher  $p_{Ar}$ , the S 2p relative intensity is distinctly lower than that of O 1s. These results suggest that Co oxidation decreases with decreasing Co–S linkages at the Co/BPDT interface.

Raman spectra from Co/BPDT/Co sandwiches (Fig. 8) exhibit the following signatures of BPDT:<sup>24,42–44</sup> C=C stretching ( $1590\text{ cm}^{-1}$ ), C–C stretching ( $1288\text{ cm}^{-1}$ ) between, and C–H bending ( $1201\text{ cm}^{-1}$ ) within, the aromatic rings, and S–C stretching ( $1078\text{ cm}^{-1}$ ). The lack of an observable peak at  $376.6\text{ cm}^{-1}$  indicates –SH moieties did not react with each other to form disulfides. These suggest that the sputter-deposition of a Co overlayer does not destroy the BPDT structure, consistent with MNLs being resilient to  $\sim 10\text{ eV}$  projectiles.<sup>45</sup>

## Conclusions

Results of our studies on nanolayered Co/BPDT/Co sandwiches provide valuable insights for the design and synthesis of nanolayered hybrid inorganic–organic laminates. In particular, our results reveal MNL-induced roughening of Co overlayers, which increases with the Ar pressure  $p_{Ar}$  during sputter deposition. It appears that the MNL accentuates self-shadowing of low mobility Co adatoms. This effect is more pronounced at higher  $p_{Ar}$  wherein increased gas-phase collisions result in low-energy Co fluxes impinging on the surface at shallow angles. Furthermore, MNL-induced Co layer roughening is correlated with a higher degree of Co oxidation, pointing to the importance of the  $p_{Ar}$  in controlling both the morphology and the chemistry of sputtered metal films on the MNL-covered surfaces. These results also suggest that the nature and extent of MNL-induced  $p_{Ar}$ -oxidation and  $p_{Ar}$ -roughness correlations are likely to be related to the MNL chemistry and morphology. This knowledge should be important for the design and synthesis of inorganic–organic nanolaminates with emergent properties, *e.g.*, transparent electrical conductors, flexible thermoelectrics, and smart materials with mechanical bandgaps.

## Conflicts of interest

There are no conflicts to declare.

## Acknowledgements

We gratefully acknowledge funding from the US National Science Foundation through the CMMI 2135725 grant, the Swedish Government Strategic Research Area in Materials Science on Advanced Functional Materials Grant SFO-Mat-LiU No. 2009 00971, the Knut and Alice Wallenberg foundation through the Wallenberg Academy Fellows Grant KAW-2020.0196 and Wallenberg Academy Scholar Grant KAW-2019.0290, and the Swedish Research Council through the VR 2021-03826 grant.

## References

- 1 G. Ramanath, C. Rowe, G. Sharma, V. Venkataramani, J. G. Alauzun, S. Ravishankar, P. Keblinski, D. G. Sangiovanni, P. Eklund and H. Pedersen, *Appl. Phys. Lett.*, 2023, **122**, 260502.
- 2 International Roadmap for Devices and Systems (IRDSTM) 2022 Edition, More Moore, <https://irds.ieee.org/editions/2022>, 2022.
- 3 C. Joachim, J. K. Gimzewski and A. Aviram, *Nature*, 2000, **408**, 541–548.
- 4 C. Wan, X. Gu, F. Dang, T. Itoh, Y. Wang, H. Sasaki, M. Kondo, K. Koga, K. Yabuki, G. J. Snyder, R. Yang and K. Koumoto, *Nat. Mater.*, 2015, **14**, 622–627.
- 5 J.-P. Niemelä, A. Philip, N. Rohbeck, M. Karppinen, J. Michler and I. Utke, *ACS Appl. Nano Mater.*, 2021, **4**, 1692–1701.
- 6 S. K. Arya, P. R. Solanki, M. Datta and B. D. Malhotra, *Biosens. Bioelectron.*, 2009, **24**, 2810–2817.
- 7 B. Yoon, B. H. Lee and S. M. George, *J. Phys. Chem. C*, 2012, **116**, 24784–24791.
- 8 D. D. Gandhi, M. Lane, Y. Zhou, A. P. Singh, S. Nayak, U. Tisch, M. Eizenberg and G. Ramanath, *Nature*, 2007, **447**, 299–302.
- 9 M. Kwan, M. Braccini, M. W. Lane and G. Ramanath, *Nat. Commun.*, 2018, **9**, 5249.
- 10 P. J. O'Brien, S. Shenogin, J. X. Liu, P. K. Chow, D. Laurencin, P. H. Mutin, M. Yamaguchi, P. Keblinski and G. Ramanath, *Nat. Mater.*, 2013, **12**, 118–122.
- 11 T. Cardinal, Devender, T. Borca-Tasciuc and G. Ramanath, *ACS Appl. Mater. Interfaces*, 2016, **8**, 4275–4279.
- 12 U. Helmersson, S. Todorova, S. A. Barnett, J. E. Sundgren, L. C. Markert and J. E. Greene, *J. Appl. Phys.*, 1987, **62**, 481–484.
- 13 R. Khadka, G. Ramanath and P. Keblinski, *Sci. Rep.*, 2022, **12**, 10788.
- 14 B. H. Lee, B. Yoon, V. R. Anderson and S. M. George, *J. Phys. Chem. C*, 2012, **116**, 3250–3257.
- 15 A. Tanskanen and M. Karppinen, *Dalton Trans.*, 2015, **44**, 19194–19199.
- 16 J. Liu, B. Yoon, E. Kuhlmann, M. Tian, J. Zhu, S. M. George, Y.-C. Lee and R. Yang, *Nano Lett.*, 2013, **13**, 5594–5599.
- 17 J. Multia and M. Karppinen, *Adv. Mater. Interfaces*, 2022, **9**, 2200210.
- 18 S. M. George, A. A. Dameron and B. Yoon, *Acc. Chem. Res.*, 2009, **42**, 498–508.
- 19 M. A. D. Millone, H. Hamoudi, L. Rodríguez, A. Rubert, G. A. Benítez, M. E. Vela, R. C. Salvarezza, J. E. Gayone, E. A. Sánchez, O. Grizzi, C. Dablemont and V. A. Esaulov, *Langmuir*, 2009, **25**, 12945–12953.
- 20 J. F. Kang, A. Ulman, S. Liao, R. Jordan, G. Yang and G.-y. Liu, *Langmuir*, 2000, **17**, 95–106.
- 21 A. Niklewski, W. Azzam, T. Strunskus, R. A. Fischer and C. Wöll, *Langmuir*, 2004, **20**, 8620–8624.



22 J.-P. Niemelä, A. J. Karttunen and M. Karppinen, *J. Mater. Chem. C*, 2015, **3**, 10349–10361.

23 Y. Du, J. Xu, B. Paul and P. Eklund, *Appl. Mater. Today*, 2018, **12**, 366–388.

24 U. Weckenmann, S. Mittler, K. Naumann and R. A. Fischer, *Langmuir*, 2002, **18**, 5479–5486.

25 A. le Febvier, L. Landälv, T. Liersch, D. Sandmark, P. Sandström and P. Eklund, *Vacuum*, 2021, **187**, 110137.

26 J. Gaube, *Ber. Bunsen-Ges.*, 1985, **89**, 352–352.

27 M. Mayer, *Max-Planck-Institut für Plasmaphysik*, 1997, Report IPP 9/113.

28 M. Mayer, *AIP Conf. Proc.*, 1999, **475**, 541–544.

29 L. G. Parratt, *Phys. Rev.*, 1954, **95**, 359–369.

30 I. Horcas, R. Fernández, J. M. Gómez-Rodríguez, J. Colchero, J. Gómez-Herrero and A. M. Baro, *Rev. Sci. Instrum.*, 2007, **78**, 013705.

31 *MultiPak*, Version 9.6.1.7, Ulvac-phi, Inc., 2015.

32 J. Stettner, L. Schwalowsky, O. H. Seeck, M. Tolan, W. Press, C. Schwarz and H. V. Känel, *Phys. Rev. B: Condens. Matter Mater. Phys.*, 1996, **53**, 1398–1412.

33 S. A. Best, P. Brant, R. D. Feltham, T. B. Rauchfuss, D. M. Roundhill and R. A. Walton, *ChemInform*, 1977, **8**.

34 X. Ma, W. Zhang, Y. Deng, C. Zhong, W. Hu and X. Han, *Nanoscale*, 2018, **10**, 4816–4824.

35 J. Yang, H. Liu, W. N. Martens and R. L. Frost, *J. Phys. Chem. C*, 2010, **114**, 111–119.

36 J.-C. Dupin, D. Gonbeau, P. Vinatier and A. Levasseur, *Phys. Chem. Chem. Phys.*, 2000, **2**, 1319–1324.

37 S. Chenakin and N. Kruse, *Appl. Surf. Sci.*, 2020, **515**, 146041.

38 M. C. Biesinger, B. P. Payne, A. P. Grosvenor, L. W. M. Lau, A. R. Gerson and R. S. C. Smart, *Appl. Surf. Sci.*, 2011, **257**, 2717–2730.

39 A. Foelske and H.-H. Strehblow, *Surf. Interface Anal.*, 2000, **29**, 548–555.

40 L. Liu, Z. Jiang, L. Fang, H. Xu, H. Zhang, X. Gu and Y. Wang, *ACS Appl. Mater. Interfaces*, 2017, **9**, 27736–27744.

41 M. Kwan, T. Cardinal, P. H. Mutin and G. Ramanath, *Appl. Phys. Lett.*, 2016, **108**, 191607.

42 Y. R. Lee, M. S. Kim and C. H. Kwon, *Bull. Korean Chem. Soc.*, 2013, **34**, 470–474.

43 S. W. Joo, S. W. Han and K. Kim, *J. Phys. Chem. B*, 1999, **103**, 10831–10837.

44 E. O. Ganbold and S. W. Joo, *Bull. Korean Chem. Soc.*, 2015, **36**, 244–249.

45 S. A. Miller, H. Luo, S. J. Pachuta and R. G. Cooks, *Science*, 1997, **275**, 1447–1450.

